1 **Drought reconstruction since 1796 CE based on tree-ring widths in the Upper**

2 **Heilongjiang (Amur) River Basin in Northeast Asia, and its linkage to Pacific**

3 **Ocean climate variability**

4 Yang Xu [1], Heli Zhang [2], Feng Chen [1]*, Shijie Wang [1], Mao Hu [1], Martín Hadad [4], Fidel Roig [5, 6]

5 *1. Yunnan Key Laboratory of International Rivers and Transboundary Eco-Security, Institute of*

6 *International Rivers and Eco-Security, Yunnan University, Kunming 650500, China*

7 *2. Key Laboratory of Tree-ring Physical and Chemical Research of China Meteorological*

8 *Administration/ Xinjiang Key Laboratory of Tree-ring Ecology, Institute of Desert Meteorology,*

9 *China Meteorological Administration, Urumqi 830002, China*

10 *3. Laboratorio de Dendrocronología de Zonas Áridas. CIGEOBIO (CONICET-UNSJ), San Juan,*

11 *Argentina, Gabinete de Geología Ambiental (INGEO-UNSJ), Av. Ignacio de la Roza 590 (oeste),*

12 *J5402DCS Rivadavia, San Juan, Argentina*

13 *4. Laboratorio de Dendrocronología e Historia Ambiental, IANIGLA-CCT CONICET, Mendoza,*

14 *Argentina*

15 *5. Hémera Centro de Observación de la Tierra, Escuela de Ingeniería Forestal, Facultad de*

16 *Ciencias, Universidad Mayor, Camino La Pirámide 5750, Huechuraba, Santiago 8580745, Chile*

17 *Correspondence: feng653@163.com

18 **Abstract:** The economic and environmental impacts of persistent droughts in East

19 Asia are of growing concern, and therefore it is important to study the cyclicity and

20 causes of these regional droughts. The self-calibrating Palmer Drought Severity Index

21 (scPDSI) has been extensively employed to describe the severity of regional drought,

22 and several PDSI reconstructions based on tree rings have been produced. We

23 compiled a tree-ring chronology for Hailar pine *(Pinus sylvestris* var. *Mongolica)*

24 from two sites in the Hailar region in the Upper Heilongjiang (Amur) River Basin.

25 Analysis of the climate response revealed that scPDSI was the primary factor limiting

tree ring growth from May to July. The mean May to July scPDSI in the Hailar region

since 1796 was reconstructed from the tree-ring width chronology. The results of

spatial correlation analysis revealed that the reconstructed scPDSI in this region

responded significantly to climate change. Analysis of the synoptic climatology

indicated that the drought in the Upper Heilongjiang (Amur) River Basin is closely

related to ENSO and the Silk Road teleconnection. The results of atmospheric water

cycle analysis show that water vapor transport processes are the dominant factor in

the development of drought in this region.

Keywords: **Tree rings; ScPDSI reconstruction; Sea surface temperature; Severe drought; Moisture recycling**

1. Introduction

Drought—accompanied by persistent high temperatures and below-average

precipitation over intervals of months to years—is of growing concern. As a natural

disaster, the frequency and duration of drought have increased as global warming has

intensified. The impact of drought on human well-being and economic productivity is

also increasing, given that drought severely threatens food and water security (Lesk et

al. 2016; Trenberth et al. 2014; Wang et al. 2016; Chen et al. 2022). Due to regional

water shortages, droughts frequently wreak havoc on agriculture and the quality of

life in northeast Asia. Hence, understanding the variability of drought in this region

and its causal mechanisms is essential for both drought prediction and the formulation

of disaster response strategies (Li et al. 2019; Yuan and Wood 2013).

However, only short-duration instrumental records of drought variability are

available for northeast Asia, most of them from the 1950s onwards. However, this deficiency can be addressed via proxy paleoclimate records, such as tree-ring widths (Fritts, 1991). With their high annual precision and extensive coverage, tree rings have been used as a reliable proxy for reconstructing historical climatic and hydrological changes (Cook et al. 2016; Chen et al. 2021; Pearson et al. 2020). Hailar is located in the Upper Heilongjiang (Amur) River Basin, in the woodland-steppe interface of northeast Asia, part of the eastern edge of the Hulunbuir grasslands, a region highly susceptible to climatic and environmental changes and that has experienced drought over the past few decades (Zhang et al. 1997; Wang et al. 2010; Bao et al. 2015; Chen et al. 2012). Drought reconstructions based on tree-ring widths can potentially make a valuable contribution to regional planning and ecological conservation in this region. Over the past two decades, several studies based on tree-ring width have been conducted in Northeast Asia (Cook et al. 2010; Bao et al. 2015; Chen et al. 2012; Liu et al. 2016; Chen et al. 2022, Zhao et al. 2023). However, there is a requirement to focus research efforts on the agro-pastoral zone located in the western region of the northeast Asia. This area is characterized by a delicate ecological balance and high climate susceptibility, making it imperative to enhance our comprehension of drought patterns and underlying mechanisms.

Severe drought events are a serious problem in northern China, especially since the late 1970s, when the weakening of the East Asian Summer Monsoon (EASM) contributed to the 'southern flooding and northern drought' climatic pattern, with frequent intense drought events in the north (Wang, 2002; Yu et al. 2004; Ding et al.

70 2009). Regarding the climatic mechanisms responsible for the northeast Asia drought,

71 it has been suggested that variations in the Pacific Ocean interdecadal oscillation

72 (PDO) and in Arctic Ocean sea-ice cover have contributed to an interdecadal decrease

73 in precipitation in northeast Asia, leading to drought (Han et al. 2015). It has also been

74 suggested that the global distribution of sea surface temperature and ENSO events are

75 closely linked to summer precipitation in northeast Asia, thus explaining the summer

76 drought mechanism in the northeast Asia from an interannual perspective (Han et al.

77 2017). Winter NAO has also been shown to impact the interannual variability of

78 summer drought events in northeast Asia (Fu and Zeng, 2005). Anticyclonic

79 circulation anomalies can often trigger extreme and prolonged drought events. Such

80 anomalies always occur as a major product of specific remote teleconnection patterns,

81 called stationary wave patterns (Schubert et al. 2014). Several steady wave models

82 have been shown to generate extreme drought events, with the 2014 summer drought

83 in northern China attributed to the European Union pattern. It has also been confirmed

84 that the Silk Road, Pacific-Japanese, and European Union models caused the

85 July–August 2014 drought in north and northeastern China (Wang and He, 2015;

86 Wang et al. 2017; Xu et al. 2017). While many of the above studies describe water

87 vapor flux anomalies during periods of extreme drought, our understanding of the role

88 of water vapor derived from local evaporation and advective transport is limited.

89 Quantifying the contribution of advected water vapor transport and precipitation

90 circulation processes to precipitation is essential for understanding the water vapor

91 cycle and anticipating the intensity of severe drought episodes (Findell and Eltahir,

92   2003; Guan et al. 2022).

93   The objectives of the present study are: (1) to reconstruct the scPDSI of the Hailar

94   region and to analyze changes in the temporal variations of regional drought; (2) to

95   determine the atmospheric circulation mechanisms generating extreme drought events;

96   and (3) to analyze the contribution of advective water vapor transport and local

97   evaporation to precipitation during droughts, and to determine their leading causes.

98   ## 2. Materials and Methods

99   ### 2.1 Study area

100 Tree-ring sampling sites NEGC (119°36′ E, 47°58′ N, 600-700m a.s.l.) and MGET

101 (119°24′ E, 47°59′ N, 1100-1200 m a.s.l.) are located in the Upper Heilongjiang

102 (Amur) River Basin (Fig. 1). The region lies within the arid and semi-arid region of

103 Northeast China (NEC), on the eastern edge of the Hulunbeier steppe and close to the

104 western slopes of the Greater Khingan Range. This region has a continental and

105 monsoonal climate (Bao et al. 2012). Due to the incursion of high-latitude cold and

106 dry air masses in winter and of warm and moist air masses from low-latitude areas in

107 summer, the climate tends to alternate between cold and dry in winter and warm and

108 humid in summer. The average annual temperature is around -0.9 °C and the average

109 yearly precipitation is ~382.8 mm (Fig. 2a). December–January is the coldest period,

110 with sparse rainfall, while June–August is the hottest period when precipitation is

111 abundant (Fig. 2b). Thus, the climate is generally cold and dry. The grassland in this

112 region is undergoing severe desertification and degradation in response to global and

113 regional climate change (Zhang et al. 2011).

2.2 Tree-ring data

The dominant tree species in the Hailar region is Hailar pine (*Pinus sylvestris* var. *Mongolica*), which was sampled for tree-ring analysis. Both sites were located at the upper tree line, on steep slopes with thin soils. Information about the sampling sites is given in Table 1. Samples were taken from breast height using a 10-mm diameter incremental borer. Forty cores were collected from 20 trees at sampling site NEGC, and 63 cores were collected from 33 trees at sampling site MGET. In the laboratory, the core samples were dried, mounted and successively sanded with 320- and 600-grit sandpaper until the tree-ring widths were visible, and were then imaged using a high-precision scanner. Tree-ring width data were measured using CooRecorder 9.4 software, and the data quality was checked by cross-matching using the quality control program COFFCHA (Holmes, 1983). The ARSTAN procedure was then used to remove non-climatic influences on the tree-ring width data, due to age and growth, using exponential detrending. This procedure resulted in a standardized chronology of tree-ring widths (STD), a chronology of differences (RES), and an autoregressive chronology (ARS). The individual detrended chronologies from the two sites were combined to produce a new RC chronology using a robust averaging method (Cook, 1985). The STD chronology was selected to retain high and low-frequency variations based on the considerations of subsequent analyses. The data series were truncated according to thresholds of at least EPS > 0.85 and 6 (3 trees) for the expressed population signal and sample size, respectively, resulting in a reliable reconstruction for the period of 1796–2020.

2.3 Climate data and statistical methods

Monthly instrumental climate data from Hailar meteorological station (49°15′ E, 119°42′ N, 650 m a.s.l.), affiliated to the National Meteorological Administration of China, including monthly mean temperature and monthly total precipitation, were obtained for the period of 1951–2020. Monthly mean runoff data from Khabarovsks Hydrological Station on the lower Heilongjiang River were used to analyze the response of the reconstructed scPDSI to runoff variations. The locations of the meteorological and hydrological stations are shown in Fig. 2a. scPDSI gridded climate data of CRU TS 4.06 from the Climate Research Unit (CRU) of the University of East Anglia were also used in this study (Harris et al. 2014). SPSS 22.0 was used to assess the correlation coefficient of the climate signals contained in the three chronologies for the individual months from July of the previous year to September of the current year. Based on the results of this correlation coefficient analysis, several seasonal climate combinations from July of the last year to September of the current year were filtered, and the seasonal climate combinations with the highest correlation were selected for climate reconstruction, using one-dimensional linear regression. A split calibration-verification test was used to test the reliability of the reconstructed models, dividing the period of 1951–2020 into independent calibration and validation periods. The main parameters assessed were the correlation coefficient (R), explained variance (R^2), efficiency coefficient (CE), error reduction value (RE), sign test (ST1), and the first-order difference sign test (ST2) (Cook and Kairiukstis, 2013). In this study, after 15-year low-pass filtering,

158   intervals of more than 10 years below/above the mean of the reconstructed series were

159   defined as dry/wet periods, and the years below or above 1.5 times the standard

160   deviation of the series mean were defined as extreme dry/wet years. The

161   quasi-periodic characteristics of the reconstructed scPDSI were analyzed using

162   Multitaper spectral analysis (MTM) (Mann and Lees, 1996). Spatial correlation maps

163   were generated between the reconstructed scPDSI series and the grid data, including

164   precipitation and scPDSI data from CRU TS 4.06, and runoff grid point data from

165   G-RUN (Harris et al. 2014; Ghiggi et al. 2021).

2.4 Land-atmosphere water balance

167   The Brubaker binary model has been used to quantify the contribution of external

168   water vapor transport and local evaporative water vapor to precipitation, based on the

169   atmospheric water vapor balance (Brubaker et al. 1993). The water vapor equation for

170   the vertical integration per unit area can be expressed as follows (Brubaker et al. 1993;

171   Guo et al. 2018):

$$\frac{\partial Q}{\partial t} = -\left(\frac{\partial F_u}{\partial x} + \frac{\partial F_v}{\partial y}\right) + E - P, \tag{1}$$

172   Where Q is the vertically integrated water vapor concentration; F_u and F_v are the

173   vertically integrated latitudinal and meridional water vapor fluxes, respectively; and E

174   and P are the vertically integrated land evaporation and rainfall, respectively.

175   Compared to the magnitude of the water vapor flux, the vertically integrated water

176   vapor content varies very little over time and is insignificant on longer timescales

177   (Burde and Zangvil, 2001). Thus, the left side of equation (1) is 0. In addition, the

water vapor balance equation for the external water vapor transport term is as follows

(Guo et al. 2018; Zhao and Zhou, 2021; Li et al. 2020):

$$-\left(\frac{\partial F_u^a}{\partial x} + \frac{\partial F_v^a}{\partial y}\right) = P_a \tag{2}$$

Where F_u^a and F_v^a represent the vertically integrated latitudinal and longitudinal

water vapor transport from external inputs, respectively. Assuming P, E and P_a are

constant within the study area during the interval of concern (Burde and Zangvil,

2001). Assuming that externally imported water vapor and locally evaporated water

vapor are well mixed over the study area, and that the proportions of evaporated and

advected water vapor contribute equally to the development of precipitation and

moisture fluxes. Using the above assumptions and the Gaussian scattering

assumptions, equations (1) and (2) can be applied to a region of area A (in m), as

follows:

$$-\left(\frac{\partial F_u}{\partial x} + \frac{\partial F_v}{\partial y}\right)|A = F_{in} - F_{out} = (P - E)A \tag{3}$$

$$-\left(\frac{\partial F_u^a}{\partial x} + \frac{\partial F_v^a}{\partial y}\right)|A = F_{in} - F_{out-a} = P_a A \tag{4}$$

Here, $-\left(\frac{\partial F_u}{\partial x} + \frac{\partial F_v}{\partial y}\right)|A$ and $-\left(\frac{\partial F_u^a}{\partial x} + \frac{\partial F_v^a}{\partial y}\right)|A$ represent the total water vapour

irradiation dispersion in the targeted region and the irradiation dispersion of externally

transported water vapor, respectively; F_{out} and F_{out-a} represent the total water

vapour leaving the calculated area and the part of the external input water vapour

flowing away from the calculated area again, respectively; and F_{in} represents the

total water vapor transported to the targeted area from outside. This enables an

estimate to be made of the contribution of external moisture transport and local land

surface evaporation to precipitation, as follows (Guo et al. 2018; Li et al. 2020):

$$r = \frac{P_a}{P} = \frac{2F_{in}}{2F_{in} + EA} \tag{5}$$

$$\rho = 1 - \frac{P_a}{P} = \frac{EA}{2F_{in} + EA} \tag{6}$$

197   Where r and ρ are the contributions to precipitation from external water vapor

198   transport and local land surface evaporation, respectively, and ρ is the precipitation

199   recirculation rate.

200   The Brubaker binary model water vapor transport process is based mainly on

201   advection terms, which can be applied to calculate the precipitation recirculation rates

202   in the study area. Give that the calculation of these precipitation recirculation rates

203   depends on the size of the selected area, the study area was enlarged (42.5–52.5°

204   N,115–125° E) for the purpose of calculation.

205   **3. Results**

206   **3.1 scPDSI reconstruction**

207   All the tree ring chronologies show a high mean sensitivity and standard

208   deviation, typical of trees growing in arid and semi-arid regions, due to the location of

209   the Hailar region. The high inter-series correlation coefficient suggests that our

210   tree-ring width chronology reliably captures several standard climate signals. The

211   EPS of the RC chronology passed the test for signal strength (EPS > 0.85) after 1796

212   (Table 2 and Fig. 3). The tree-ring width series has a significant negative correlation

213   with temperature, a significant positive correlation with precipitation, and a

214   significant positive correlation with scPDSI, according to the climate response results

215   (p < 0.05) (Fig. 4a, b). Screening for seasonal combinations of temperature,

216   precipitation, and scPDSI revealed the strongest correlation coefficien between the

217 RC tree ring width chronology and meant scPDSI from May to July (r = 0.645, p <

218 0.01). Accordingly, we reconstructed the May to July scPDSI for the Hailar region

219 since 1796 CE, using the following equation (Fig. 4d):

$$Y = 3.681X - 4.146 \tag{7}$$

$$(n = 70, \; r = 0.645, R^2 = 41.6\%, R^2_{adj} = 40.7\%, F = 48.385, p < 0.01)$$

220 Where Y is the mean reconstructed scPDSI for May to July, and X is the tree ring

221 width index from the composite chronology.

222 In equation (7), the correlation between the mean May–July scPDSI and the

223 tree-ring width index over the period of 1951–2020 is 0.645, with the tree-ring width

224 index explaining 41.6% (40.7% after adjustment for the degrees of freedom) of the

225 mean scPDSI variance, $F = 48.385$ and $p < 0.01$. Except for several anomalously high

226 values, the reconstructed mean scPDSI values agree well with the instrumental data

227 (Fig. 4c). The first-order differencing correlation coefficient is 0.571. The split

228 calibration-verification test results show that the reconstruction model has good

229 reliability and stability, with values of RE and CE > 0.20. The sign and first-order

230 difference sign tests are significant at the 0.05 level (Table 3). These results suggest

231 that our scPDSI reconstruction has reliably recorded climate signals.

232 **3.2 Characteristics of the scPDSI reconstruction**

233 Our scPDSI reconstructions reveal oscillations between drier and wetter conditions

234 in the Hailar region during 1796–2020 CE (Fig. 4e). Dry/wet periods after 15-year

235 low-pass filtering were continuously below/above the long-term mean for more than

236 10 years. Four dry periods (1809–1819, 1829–1878, 1937–1950, 1990–2012), and

237 five wet periods (1796-1808, 1879-1900, 1910-1936, 1951-1963, 1970-1989) are

238 evident in the record. A data value < 1.5 times the standard deviation of the long-term

239 mean is defined as an extreme drought year, and such years occurred in 1779, 1826,

240 1837, 1840, 1842, 1857, 1864, 1866, 1951, 1996 and 2007. The curves also show an

241 increase following lower values in the 1870s, and a clear decreasing trend in the last

242 10 years, which is consistent with the instrumental observations (Fig. 4e). The results

243 of the MTM analysis revealed periodicities of 2–8.1 years (Fig. 5). The results of

244 spatial correlation analysis revealed a strong positive correlation between the

245 reconstructed scPDSI series on the scale of the upper basin of the Heilongjiang (Amur)

246 River and the gridded scPDSI, total rainfall, and runoff, from May to July (Fig. 6a, b).

247 After obtaining the mean series of the gridded data, good correlation coefficiens were

248 obtained between the reconstructed scPDSI and the regional mean of the gridded data,

249 with $r = 0.57$ ($p < 0.01$), and $r = 0.35$ ($p < 0.01$), with CRU scPDSI and CRU

250 precipitation, respectively (Fig. 6a, b, c). The correlation coefficiens between

251 reconstructed scPDSI and G-RUN runoff and runoff from the Khabarovsks

252 Hydrological Station runoff were $r = 0.34$ ($p < 0.01$) and $r = 0.36$ ($p < 0.01$),

253 respectively (Fig. 6d). These results indicate that our scPDSI reconstructions reliably

254 reflect the regional drought characteristics and changes in runoff in the Upper

255 Heilongjiang (Amur) River Basin.

256 **4. Discussion**

257 **4.1 Climate–tree ring growth relationships and temporal variations**

258 **in regional drought**

259   The positive correlation between tree-ring width and rainfall and the negative

260   correlation with temperature indicate that the increase in the circumference of *P.*

261   *sylvestris var. Mongolica* in the Hailar area is described by a humidity-sensitive

262   growth model. Temperature is much a greater stressor for tree growth in arid and

263   semi-arid regions than precipitation (Bao et al. 2015; Fang et al. 2010; Sun et al.

264   2012). The higher correlation coefficiens between temperature and the tree-ring

265   indices in our dataset   indicate that the radial expansion of *P. sylvestris* var.

266   *Mongolica* in the Hailar region is   mainly influenced by soil moisture conditions

267   modulated by temperature variations (Fig. 4a). Compared with precipitation alone,

268   PDSI better reflects changes in soil moisture caused by precipitation and temperature

269   stress on the radial growth of trees. The PDSI during the growing season from May to

270   July also shows the highest correlation with scPDSI ($r = 0.645$, $p < 0.01$) (Fig. 4c).

271   The radial growth of *P. sylvestris* var. *Mongolica* is mainly determined by the control

272   of soil moisture by precipitation (Song et al. 2015). However, in semiarid areas, the

273   increasing temperature during the growing season accelerates the evaporation of soil

274   moisture and enhances plant transpiration, and thus the soil moisture supply is

275   insufficient for tree growth (Shang et al. 2012). In contrast, temperatures above a

276   certain threshold during the growth season can adversely affect tree growth because

277   the decrease in the net photosynthetic rate and excessive temperatures will lead to

278   more severe drought stress (D'arrigo et al. 2004).

279   The reconstructed scPDSI reveals ten extreme drought years during 1796–2000,

280   seven of which can be identified in historical documents (Zhang, 2004; Liu and Wen,

281 2008). (Table 4). The historical literature includes detailed descriptions of drought

282 events; for example, 1951 was a drought year throughout Inner Mongolia—one of a

283 series of relatively severe droughts—when the lack of rainfall in summer and autumn

284 was more severe than in spring. Numerous seedlings of crop plants in Hulunbuir were

285 killed by the drought and the grain yield of the entire region was significantly reduced

286 (Liu and Wen, 2008). In 1996, a severe drought affected the north-central part of Inner

287 Mongolia in early summer (Liu and Wen, 2008). Our reconstruction captures several

288 extreme drought events in the past decade. The intense heat in NEC during

289 July–August 2016 resulted in severe crop yield reductions and economic losses

290 amounting to $15,61 billion (Li et al. 2018). In 2017, the Northeast China (NEC)

291 region encountered an exceptionally severe spring and summer drought event (Zeng

292 et al. 2019). This event had a significant impact on the cultivated area in eastern Inner

293 Mongolia. Notably, the crop failure extent and ensuing economic losses ranked as the

294 second highest since 2012. The drought affected an area of 74.3×104 km2 across the

295 region, with the western Hulunbuir area experiencing primarily moderately intense

296 drought (Zhang et al. 2017).

297 **4.2 Synoptic meteorological analysis of severe drought**

298 To explore the climatic drivers of the extreme drought events, we screened the

299 wettest and driest decades from 1891 to 2020. SST changes in the previous winter are

300 critical for precipitation in East Asia in the following year (Juneng and Tangang,

301 2005), and thus we selected the winter SST from December of the previous year to

302 January of the current year to analyze the respective decadal SST anomalies. The

303 results indicate that during wet years, SST has the negative ENSO phase pattern,

304 while in dry years, it has the positive ENSO phase pattern (Fig. 7a, b). The

305 reconstructed scPDSI also has the same 2–5 year cycle as ENSO (Fig. 5), suggesting

306 that ENSO may have contributed to drought in the Upper Heilongjiang (Amur) River

307 Basin. The wettest decade and the driest decade from 1950 to 2020 were also selected

308 for climatological analysis, which revealed the following relationships. During the

309 wet years, the SST in the preceding winter had the negative ENSO phase pattern, the

310 SST in the eastern equatorial Pacific decreased, and the western Pacific warm pool

311 and the Walker circulation intensified. At the same time, the western Pacific

312 subtropical high pressure weakened and shifted northward, the Mongolian high

313 pressure weakened significantly (Fig. 8a), the anomalous cyclone in the wet years

314 corresponded to a cold anomaly (Fig. 8c), and the major rainfall band in May–July

315 (MJJ) shifted northward. This scenario caused an anomalous increase in precipitation

316 in the Upper Heilongjiang (Amur) River Basin during the selected wet years. In dry

317 years, the SST in the preceding winter had an ENSO positive phase pattern, the SST

318 difference between the western and eastern equatorial Pacific decreased, the

319 latitudinal Walker circulation weakened, the western Pacific subtropical high pressure

320 strengthens and shifted southward compared to normal. These events result in weak

321 East Asian summer winds and a significantly more intense Mongolian high (Fig. 8b).

322 The anomalous cyclone in dry years corresponds to a warm anomaly (Fig. 8d), and

323 the anticyclone corresponds to a warm anomaly (Fig. 8d), which is controlled by an

324 eccentric northerly component that favors cold air transport from high latitudes to the

325 northeast during dry years. This results in anomalous descending motion and a

326 southward shift of the main rain and wind belts, leading to drought (Fig. 8f).

327 Several additional studies have found that Nino3 SST has a significant negative

328 correlation with precipitation in North China (Wang 2002, Yu et al. 2004), and the

329 negative correlation between rainfall and ENSO in northern China is associated with

330 anomalous cyclones over East Asia (Wu, Hu et al. 2003). These findings exhibit

331 congruence with the outcomes derived from our analytical examinations. In summary,

332 the large-scale ocean-atmosphere-land circulation system is a critical driver of

333 drought development in the Upper Heilongjiang (Amur) River Basin.

334 ## 4.3 Atmospheric water cycle during drought years

335 Based on NCEP-NCAR reanalysis 1 data (Kalnay et al. 1996), we quantified the

336 meteorological conditions and atmospheric hydrological cycle anomalies in the Hailar

337 region during May–July of the driest decade of 1950–2020, based on the

338 reconstructed scPDSI. The total climatic precipitation for May–July of 1950–2020

339 was 27.0×10^6 kg/s, while the total precipitation for May–July in a drought year was

340 23.0×10^6 kg/s, a decrease of 14.8%. The external advective input (F_{in}) under

341 climatic conditions was 230.9×10^6 kg/s, compared to 211.4×10^6 kg/s during the dry

342 year, with an 8.4% reduction in external advective input during the drought.

343 Evaporation (E) was 30.7×10^6 kg/s under these climatic conditions, and 29.5×10^6

344 kg/s during dry years, with a 3.9% reduction in evaporation during the drought.

345 Precipitation formed by external advective input (P_a) under these climatic conditions

346 was 25.3×10^6 kg/s, contributing 93.8% to precipitation, and precipitation formed by

347 evaporation (P_e) was 1.7×10^6 kg/s, with a precipitation recirculation rate of 6.2%.

348 Precipitation formed by external advection input (P_a) during the dry year was $21.4 \times$

349 10^6 kg/s, contributing 93.5% to precipitation, and precipitation formed by evaporation

350 (P_e) was 1.5×10^6 kg/s, with the precipitation recirculation rate of 6.5% (Fig. 9b).

351 During the dry year, total precipitation decreased by 14.8% compared to the climatic

352 mean, and the external advective input of water vapor decreased significantly (8.4%),

353 resulting in a 15.4% decrease in precipitation formed from the external advective

354 input of water vapor, with little change in evaporation and precipitation formed by

355 evaporation. These results suggest that the drought in the Upper Heilongjiang (Amur)

356 Basin is mainly caused by a reduction in the external advective water vapor input

357 rather than by anomalies in the precipitation cycle. Synthetic anomalies in the whole

358 layer water vapor fluxes and precipitation rates also indicate a decrease in advective

359 water vapor transport and precipitation during the drought (Fig. 9a). These results

360 indicate that variations in the process of moisture transport play a pivotal role in the

361 formation of drought in the Upper Heilongjiang (Amur) River Basin.

5. Conclusion

363 We built a composite tree-ring chronology for two sampling sites in the Hailar

364 region. Based on this chronology, we reconstructed the monthly mean scPDSI for

365 May–July in the Upper Heilongjiang (Amur) Basin since 1796. the reconstructed

366 sequence comprises more than 220 years of wet and dry variations in the Upper

367 Heilongjiang (Amur) River Basin, which experienced four consecutive dry periods

368 and five consecutive wet periods,   since 1796 CE, with a significant 2-8-year

cyclicity. The drought reconstruction accurately captured the recent trends in dry/wet variability and it reflects drought variability across a large area.

Our synoptic climatological analysis of extreme drought years suggests that the dry/wet variability in the Upper Heilongjiang (Amur) River Basin is related to several large-scale climate stresses and atmospheric circulation patterns (the ENSO and Silk Road models), and that one of the critical drivers of drought development in the Upper Heilongjiang (Amur) River Basin is the large-scale ocean-atmosphere-land circulation system. Our atmospheric water circulation analysis suggests that the cause of drought is primarily a reduction in advective water vapor transport, rather than precipitation circulation processes, which further implies that atmospheric circulation systems control wet/dry variability in the Upper Heilongjiang (Amur) River Basin.

Our drought reconstruction has several shortcomings since it is based on only two sample sites, and it spans a relatively short interval (230 years), and represents only a very small region. Therefore, it is essential to systematically compile additional tree ring–based climate records from this region to provide drought reconstructions on a large spatial scale, which may help characterize the spatio-temporal variability and impact mechanisms of drought within NEC.

References

Bao, G., et al.: "April-September mean maximum temperature inferred from Hailar pine (Pinus sylvestris var. mongolica) tree rings in the Hulunbuir region, Inner Mongolia, back to 1868 AD." Palaeogeography Palaeoclimatology Palaeoecology 313: 162-172. https://doi.org/10.1016/j.pala

391   eo.2011.10.017, 2012.

392   Bao, G., Liu, Y., Liu, N., and Linderholm, H. W.: Drought variability in eastern Mongolian Plateau and

393   its linkages to the large-scale climate forcing, Climate Dynamics, 44, 717-733, https://doi.org/

394   10.1007/s00382-014-2273-7, 2015.

395   Brubaker, K. L., Entekhabi, D., and Eagleson, P. S.: ESTIMATION OF CONTINENTAL

396   PRECIPITATION RECYCLING, Journal of Climate, 6, 1077-1089,

397   https://doi.org/10.1175/1520-0442(1993)006<1077:Eocpr>2.0.Co;2, 1993.

398   Burde, G. I. and Zangvil, A.: The estimation of regional precipitation recycling. Part I: Review of

399   recycling models, Journal of Climate, 14, 2497-2508, https://doi.org/10.1175/1520-

400   0442(2001)014<2497:Teorpr>2.0.Co;2, 2001.

401   Chen, F., Opala-Owczarek, M., Khan, A., Zhang, H. L., Owczarek, P., Chen, Y. P., Ahmed, M., and

402   Chen, F.: Late twentieth century rapid increase in high Asian seasonal snow and glacier-derived

403   streamflow tracked by tree rings of the upper Indus River basin, Environmental Research Letters,

404   16, https://doi.org/10.1088/1748-9326/ac1b5c, 2021.

405   Chen, F., Martin, H., Zhao, X., Roig, F., Zhang, H. L., Wang, S. J., Yue, W. P., and Chen, Y. P.:

406   Abnormally low precipitation-induced ecological imbalance contributed to the fall of the Ming

407   Dynasty: new evidence from tree rings, Climatic Change, 173,

408   https://doi.org/10.1007/s10584-022-03406-y, 2022.

409   Chen, Z. J., Zhang, X. L., Cui, M. X., He, X. Y., Ding, W. H., and Peng, J. J.: Tree-ring based

410   precipitation reconstruction for the forest-steppe ecotone in northern Inner Mongolia, China and

411   its linkages to the Pacific Ocean variability, Global and Planetary Change, 86-87, 45-56,

412   https://doi.org/10.1016/

413   j.gloplacha.2012.01.009, 2012.

414   Cook, B. I., Anchukaitis, K. J., Touchan, R., Meko, D. M., and Cook, E. R.: Spatiotemporal drought

415   variability in the Mediterranean over the last 900years, Journal of Geophysical

416   Research-Atmospheres, 121, 2060-2074, https://doi.org/10.1002/2015jd023929, 2016.

417   Cook, E. R.: A time series analysis approach to tree ring standardization, University of Arizona Tucson,

418   1985.

Cook, E. R. and Kairiukstis, L. A.: Methods of dendrochronology: applications in the environmental sciences, Springer Science & Business Media, 2013.

Cook, E. R., Anchukaitis, K. J., Buckley, B. M., D'Arrigo, R. D., Jacoby, G. C., and Wright, W. E.: Asian Monsoon Failure and Megadrought During the Last Millennium, Science, 328, 486-489, https://doi.org/10.1126/science.1185188, 2010.

D'Arrigo, R. D., Kaufmann, R. K., Davi, N., Jacoby, G. C., Laskowski, C., Myneni, R. B., and Cherubini, P.: Thresholds for warming-induced growth decline at elevational tree line in the Yukon Territory, Canada, Global Biogeochemical Cycles, 18, https://doi.org/10.1029/2004gb002249, 2004.

Ding, Y. H., Sun, Y., Wang, Z. Y., Zhu, Y. X., and Song, Y. F.: Inter-decadal variation of the summer precipitation in China and its association with decreasing Asian summer monsoon Part II: Possible causes, International Journal of Climatology, 29, 1926-1944, https://doi.org/10.1002/joc.1759, 2009.

Fang, K. Y., Gou, X. H., Chen, F. H., D'Arrigo, R., and Li, J. B.: Tree-ring based drought reconstruction for the Guiqing Mountain (China): linkages to the Indian and Pacific Oceans, International Journal of Climatology, 30, 1137-1145, https://doi.org/10.1002/joc.1974, 2010.

Findell, K. L. and Eltahir, E. A. B.: Atmospheric controls on soil moisture-boundary layer interactions. Part I: Framework development, Journal of Hydrometeorology, 4, 552-569, https://doi.org/10.1175/1525-7541(2003)004<0552:Acosml>2.0.Co;2, 2003.

Fritts, H. C.: Reconstructing large-scale climatic patterns from tree-ring data: t diagnostic analysis, University of Arizona Press1991.

Fu, C. B. and Zeng, Z. M.: Correlations between North Atlantic Oscillation Index in winter and eastern China Flood/Drought Index in summer in the last 530 years, Chinese Science Bulletin, 50, https://doi.org/2505-2516, 10.1360/04wd0284, 2005.

Ghiggi, G., Humphrey, V., Seneviratne, S. I., and Gudmundsson, L.: G-RUN ENSEMBLE: A Multi-Forcing Observation-Based Global Runoff Reanalysis, Water Resources Research, 57, 2021.

Guan, Y. S., Gu, X. H., Slater, L. J., Li, L. F., Kong, D. D., Liu, J. Y., Zhang, X., and Yan, X. S.: Tracing anomalies in moisture recycling and transport to two record-breaking droughts over the

Mid-to-Lower Reaches of the Yangtze River, Journal of Hydrology, 609, https://doi.org/10.1016/j.jhydrol.2022.127787, 2022.

Guo, L., Klingaman, N. P., Demory, M. E., Vidale, P. L., Turner, A. G., and Stephan, C. C.: The contributions of local and remote atmospheric moisture fluxes to East Asian precipitation and its variability, Climate Dynamics, 51, 4139-4156, https://doi.org/10.1007/s00382-017-4064-4, 2018.

Han, T. T., Chen, H. P., and Wang, H. J.: Recent changes in summer precipitation in Northeast China and the background circulation, International Journal of Climatology, 35, 4210-4219, https://doi.org/10.1002/joc.4280, 2015.

Han, T. T., Wang, H. J., and Sun, J. Q.: Strengthened Relationship between Eastern ENSO and Summer Precipitation over Northeastern China, Journal of Climate, 30, 4497-4512, https://doi.org/10.1175/jcli-d-16-0551.1, 2017.

Harris, I., Jones, P. D., Osborn, T. J., and Lister, D. H.: Updated high-resolution grids of monthly climatic observations - the CRU TS3.10 Dataset, International Journal of Climatology, 34, 623-642, https://doi.org/10.1002/joc.3711, 2014.

Holmes, R. L.: Computer-assisted quality control in tree-ring dating and measurement, 1983.

Ishii, M., Shouji, A., Sugimoto, S., and Matsumoto, T.: Objective analyses of sea-surface temperature and marine meteorological variables for the 20th century using ICOADS and the Kobe collection, International Journal of Climatology: A Journal of the Royal Meteorological Society, 25, 865-879, 2005.

Juneng, L. and Tangang, F. T.: Evolution of ENSO-related rainfall anomalies in Southeast Asia region and its relationship with atmosphere-ocean variations in Indo-Pacific sector, Climate Dynamics, 25, 337-350, https://doi.org/10.1007/s00382-005-0031-6, 2005.

Kalnay, E., Kanamitsu, M., Kistler, R., Collins, W., Deaven, D., Gandin, L., Iredell, M., Saha, S., White, G., Woollen, J., Zhu, Y., Chelliah, M., Ebisuzaki, W., Higgins, W., Janowiak, J., Mo, K. C., Ropelewski, C., Wang, J., Leetmaa, A., Reynolds, R., Jenne, R., and Joseph, D.: The NCEP/NCAR 40-year reanalysis project, Bulletin of the American Meteorological Society, 77, 437-471, https://doi.org/10.1175/1520-0477(1996)077<0437:Tnyrp>2.0.Co;2, 1996.

Lesk, C., Rowhani, P., and Ramankutty, N.: Influence of extreme weather disasters on global crop production, Nature, 529, 84-+, https://doi.org/10.1038/nature16467, 2016.

Li, H., Chen, H., Wang, H., Sun, J., and Ma, J.: Can Barents Sea ice decline in spring enhance summer hot drought events over northeastern China?, Journal of Climate, 31, 4705-4725, 2018.

Li, Y., Zhang, L., and Wang, B.: Contributions of Local and Remote Water Vapor Transport to Precipitation Variations over Songhua River Basin, Chinese Journal of Atmospheric Sciences, 44, 611-624, 2020.

Li, Y. H., Yuan, X., Zhang, H. S., Wang, R. Y., Wang, C. H., Meng, X. H., Zhang, Z. Q., Wang, S. S., Yang, Y., Han, B., Zhang, K., Wang, X. P., Zhao, H., Zhou, G. S., Zhang, Q., He, Q., Guo, N., Hou, W., Zhang, C. J., Xiao, G. J., Sun, X. Y., Yue, P., Sha, S., Wang, H. L., Zhang, T. J., Wang, J. S., and Yao, Y. B.: Mechanisms and Early Warning of Drought Disasters: Experimental Drought Meteorology Research over China, Bulletin of the American Meteorological Society, 100, 673-687, https://doi.org/10.1175/bams-d-17-0029.1, 2019.

Liu, G. and Wen, K.: Chinese Meteorological Disasters Ceremony (Inner Mongolia Volume), 2008.

Liu, N., Liu, Y., Bao, G., Bao, M., Wang, Y. C., Zhang, L. Z., Ge, Y. X., Bao, W., and Tian, H.: Drought reconstruction in eastern Hulun Buir steppe, China and its linkages to the sea surface temperatures in the Pacific Ocean, Journal of Asian Earth Sciences, 115, 298-307, https://doi.org/10.1016/j.jseaes.2015.10.009, 2016.

Mann, M. E. and Lees, J. M.: Robust estimation of background noise and signal detection in climatic time series, Climatic change, 33, 409-445, 1996.

Pearson, C., Salzer, M., Wacker, L., Brewer, P., Sookdeo, A., and Kuniholm, P.: Securing timelines in the ancient Mediterranean using multiproxy annual tree-ring data (vol 117, pg 8410, 2020), Proceedings of the National Academy of Sciences of the United States of America, 117, 18891-18891, https://doi.org/10.1073/pnas.2013168117, 2020.

Schubert, S. D., Wang, H. L., Koster, R. D., Suarez, M. J., and Groisman, P. Y.: Northern Eurasian Heat Waves and Droughts, Journal of Climate, 27, 3169-3207, https://doi.org/10.1175/jcli-d-13-00360.1, 2014.

Shang, J., Shi, Z., Gao, J., Xu, L., Lu, S., Feng, C., and Wang, L.: Response of tree-ring width of Pinus sylvestris var.mongolica to climate change in Hulunbuir sand land,China, Acta Ecologica Sinica, 32, 1077-1084, 2012.

Song, L., Liu, B., Zhang, H., and Liu, Y.: Response of Pinus sylvestris var. mongolica Tree-ring Width to Climate Change in Hulunbuir Sandy Land,China, Journal of North-East Forestry University, 43, 17, 2015.

Sun, J. Y., Liu, Y., Sun, B., and Wang, R. Y.: Tree-ring based PDSI reconstruction since 1853 AD in the source of the Fenhe river basin, Shanxi province, China, Science China-Earth Sciences, 55, 1847-1854, https://doi.org/10.1007/s11430-012-4369-4, 2012.

Trenberth, K. E., Dai, A. G., van der Schrier, G., Jones, P. D., Barichivich, J., Briffa, K. R., and Sheffield, J.: Global warming and changes in drought, Nature Climate Change, 4, 17-22, https://doi.org/10. 10 38/nclimate2067, 2014.

Wang, H. J.: The instability of the East Asian summer monsoon - ENSO relations, Advances in Atmospheric Sciences, 19, 1-11, 2002.

Wang, H. J. and He, S. P.: The North China/Northeastern Asia Severe Summer Drought in 2014, Journal of Climate, 28, 6667-6681, https://doi.org/10.1175/jcli-d-15-0202.1, 2015.

Wang, L. Y., Yuan, X., Xie, Z. H., Wu, P. L., and Li, Y. H.: Increasing flash droughts over China during the recent global warming hiatus, Scientific Reports, 6, https://doi.org/10.1038/srep30571, 2016.

Wang, S. S., Yuan, X., and Li, Y. H.: Does a Strong El Nino Imply a Higher Predictability of Extreme Drought? Scientific Reports, 7, https://doi.org/10.1038/srep40741, 2017.

Wang, X., Zhang, C., Hasi, E., and Dong, Z.: Has the Three Norths Forest Shelterbelt Program solved the desertification and dust storm problems in arid and semiarid China?, Journal of Arid Environments, 74, 13-22, 2010.

Wu, R. G., Hu, Z. Z., and Kirtman, B. P.: Evolution of ENSO-related rainfall anomalies in East Asia, Journal of Climate, 16, 3742-3758, https://doi.org/10.1175/1520-0442(2003)016<3742:Eoerai>2.0. Co;2, 2003.

Xu, Z. Q., Fan, K., and Wang, H. J.: Role of sea surface temperature anomalies in the tropical Indo-Pacific region in the northeast Asia severe drought in summer 2014: month-to-month perspective, Climate Dynamics, 49, 1631-1650, https://doi.org/10.1007/s00382-016-3406-y, 2017.

Yu, R. C., Wang, B., and Zhou, T. J.: Tropospheric cooling and summer monsoon weakening trend over East Asia, Geophysical Research Letters, 31, https://doi.org/10.1029/2004gl021270, 2004.

Yuan, X. and Wood, E. F.: Multimodel seasonal forecasting of global drought onset, Geophysical Research Letters, 40, 4900-4905, https://doi.org/10.1002/grl.50949, 2013.

Zeng, D. W., Yuan, X., and Roundy, J. K.: Effect of Teleconnected Land-Atmosphere Coupling on Northeast China Persistent Drought in Spring-Summer of 2017, Journal of Climate, 32, 7403-7420, https://doi.org/10.1175/jcli-d-19-0175.1, 2019.

Zhang, D. e.: A compendium of Chinese meteorological records of the last 3000 years, Jiangsu Education House, Nanjing, 2004.

Zhang, G. L., Xu, X. L., Zhou, C. P., Zhang, H. B., and Ouyang, H.: Responses of grassland vegetation to climatic variations on different temporal scales in Hulun Buir Grassland in the past 30 years, Journal of Geographical Sciences, 21, 634-650, https://doi.org/10.1007/s11442-011-0869-y, 2011.

Zhang, L., Fang, X., Ren, G., and Suo, X.: Environmental changes in the North China farming-grazing transitional zone, Earth Science Frontiers, 4, 127-134, 1997.

Zhang, Y., Zhang, L., Wang, S., and Feng, J.: Drought events and their influence in summer of 2017 in China, J. Arid Meteor, 35, 899-905, 2017.

Zhao, Y. and Zhou, T. J.: Interannual Variability of Precipitation Recycle Ratio Over the Tibetan Plateau, Journal of Geophysical Research-Atmospheres, 126, https://doi.org/10.1029/2020jd033733, 2021.

Zhao, X. E., et al.: Reconstructed Jing River streamflow from western China: A 399-year perspective for hydrological changes in the Loess Plateau, Journal of Hydrology, 621, https://doi.org/10.1016/j.jhyd rol.2023.129573,2023.

Tables

Table 1. Information about the tree-ring sampling sites in the Upper Amur (Heilongjiang) River Basin.

Site code	Lat. (N)	long. (E)	Elevation (m)	Sample	Slope inclination	Exposure	Species
MGET	121°49′	46°42′	1120	63/33	5°-20°	0.2	*P sylvestris var. Mongolica*
NEGC	118°44′	49°12′	1540	40/20	10°-20°	0.3	*P sylvestris var. Mongolica*
RC				103/53			*P sylvestris var. Mongolica*

Table 2. Statistical properties of the tree-ring width chronologies from the Upper Amur (Heilongjiang) River Bas

Statistic	MGET	NEGC	RC
Mean sensitivity	0.285	0.367	0.307
Standard deviation	0.198	0.21	0.19
Mean correlation between the trees	0.658	0.723	0.653
Signal to noise ratio (SNR)	86.651	60.15	26.063
Variance of the first eigenvector (%)	58.6	66.4	38.6

Table 3. Results of verification and calibration tests for the scPDSI reconstruction.

Statistical procedure	Calibration (1951-1985)	Verification (1986-2020)	Calibration (1986-2020)	Verification (1951-1985)	Full calibration (1951–2020)
R	0.727	0.611	0.661	0.611	0.645
r^2	0.529	0.374	0.436	0.374	0.416
RE		0.357		0.491	
CE		0.378		0.566	
Sign test		24+/11-		23+/12-	
First-order sign test		22+/12-		22+/12-	

Table 4. Comparisons between the reconstructed scPDSI and documented climatic events.

Year	PDSI$_{5-7}$	Local historical documents

1779	-2.93	Famine in Taiyuan and Baotou
1837	-2.31	Drought in Qiqihaer
1842	-2.62	Drought in Baotou
1857	-2.28	Drought in Baotou and the Qingshuihe river
1866	-2.79	Drought in Hulunbuir
1951	-3.01	Inner Mongolia region drought, decrease I in Hulunbuir grain production
1996	-2.23	Drought in North Central Inner Mongolia in early summer

569

570

571

572

573

574

575

576

577

578

579

580

581

582

583

584 **Figures**
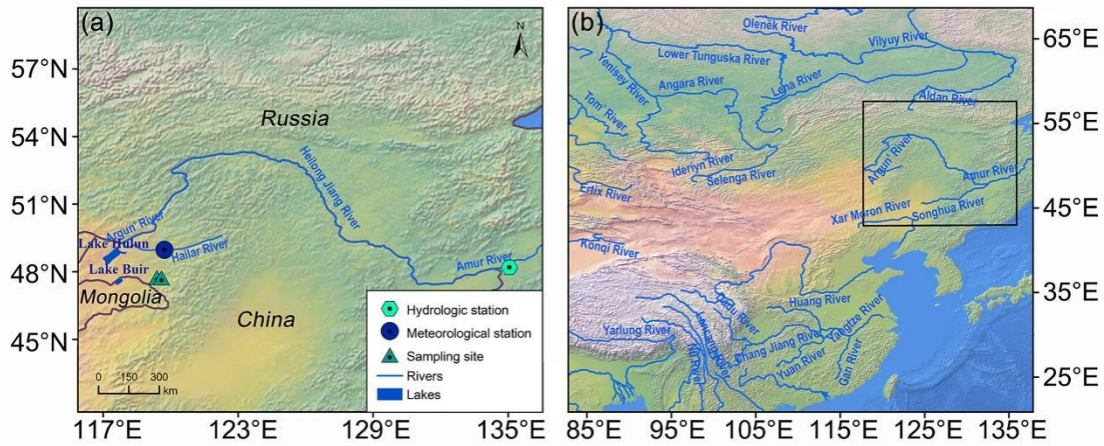
Figure 1. (a) Location of the tree-ring sampling sites, and meteorological and hydrological stations in the Upper Amur (Heilongjiang) River Basin. (b) Location of the study area in Asia. (This figure was generated using ArcGIS 10.2. The raster data for the production of the map was taken from https://www.naturalearthdata.com/)
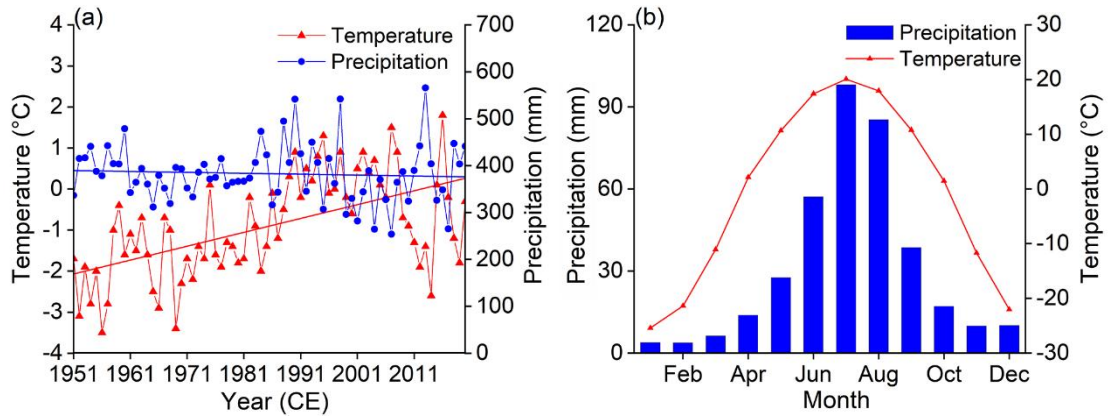
Figure 2. (a) Annual precipitation and temperature trends for the Upper Amur (Heilongjiang) River Basin from 1951 to 2020. (b) Monthly total precipitation and mean temperature for the Upper Amur (Heilongjiang) River Basin.

597
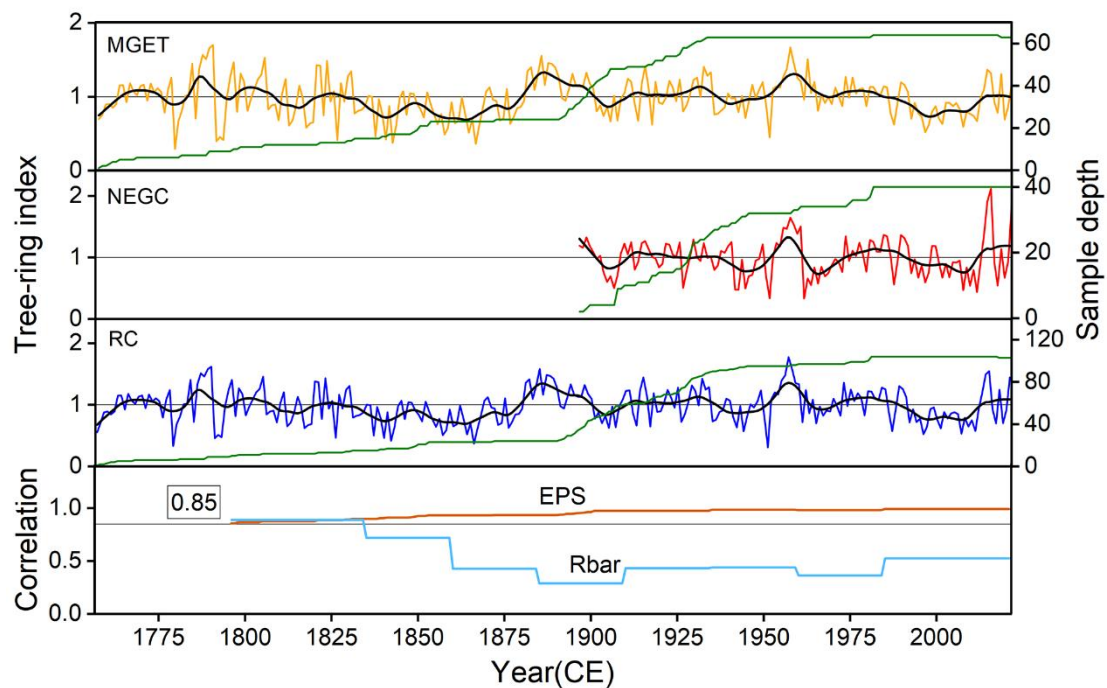
598 **Figure 3.** Chronologies of the two tree-rings records (MGET and NEGC) and the RC
599 from the Upper Amur (Heilongjiang) River Basin. The thick black curve illustrates
600 the 15-year low-pass filtered curve of the tree-ring width index. The inter-series
601 correlation (Rbar) and the EPS are shown in the lowermost panel.

602

603
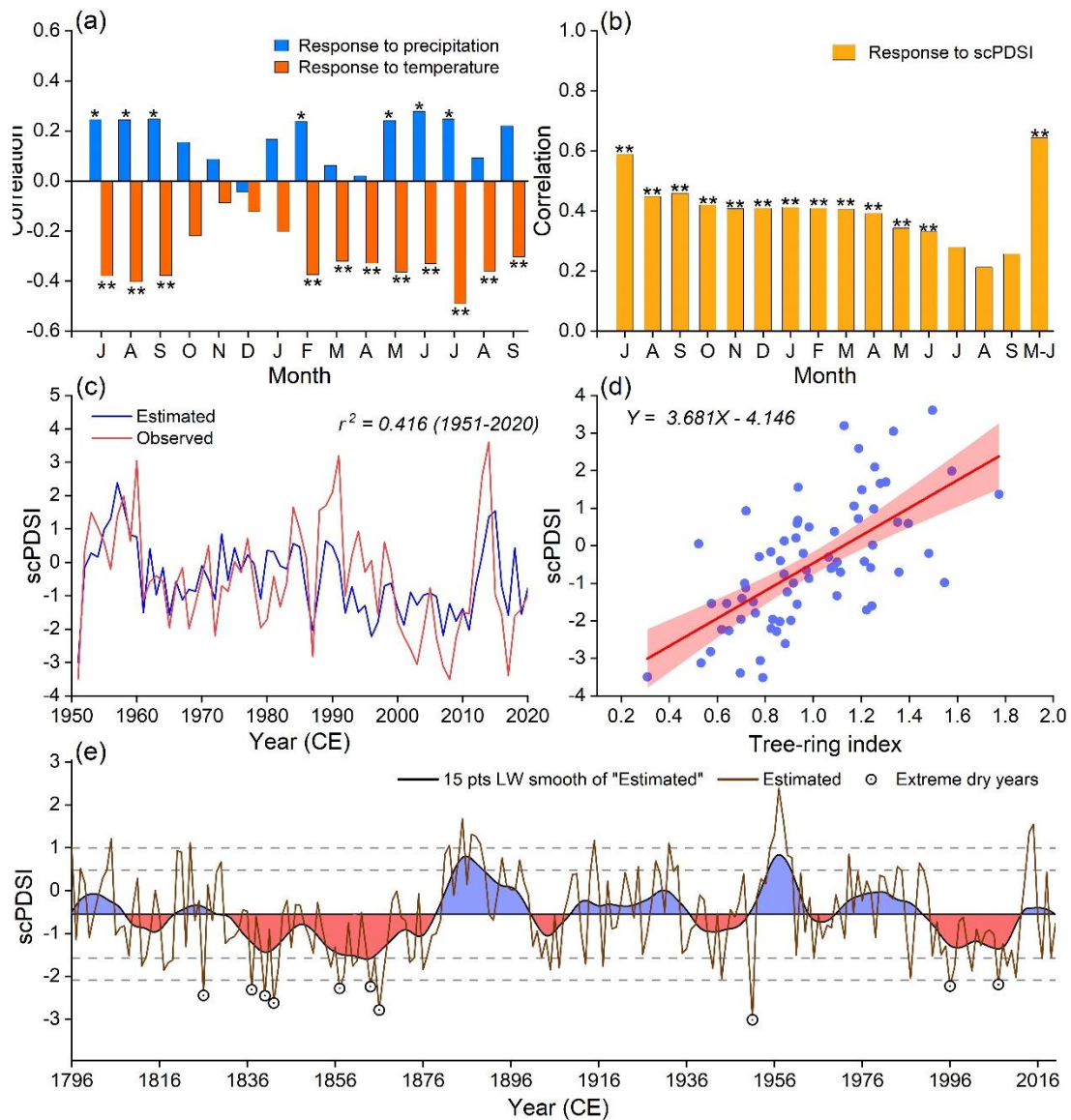
604
605 **Figure 4.** (a) Correlation coefficients between the tree-ring chronologies and monthly
606 total precipitation and mean temperature. (b) Correlation coefficients between the RC
607 tree-ring chronologies and monthly mean scPDSI of the CRU. Correlations are
608 calculated from the previous June to the current September over the time period of
609 1951–2020 (* represent the 95% significance level, and ** represents the 99%
610 significance level). (c) Comparison between the instrumental and reconstructed mean
611 May–July scPDSI for the Hailar region during 1951–2020. (d) One-dimensional
612 linear regression fits for the May to July scPDSI for 1796–2020. (e) Reconstructed
613 mean May–July scPDSI and its 15-year low-pass filtered version since 1796 CE. The
614 horizontal central line represents the average reconstructed scPDSI. The horizontal
615 dotted lines represent ±1 SD and ±1.5 SD on a mean value basis.
616
617
618

619
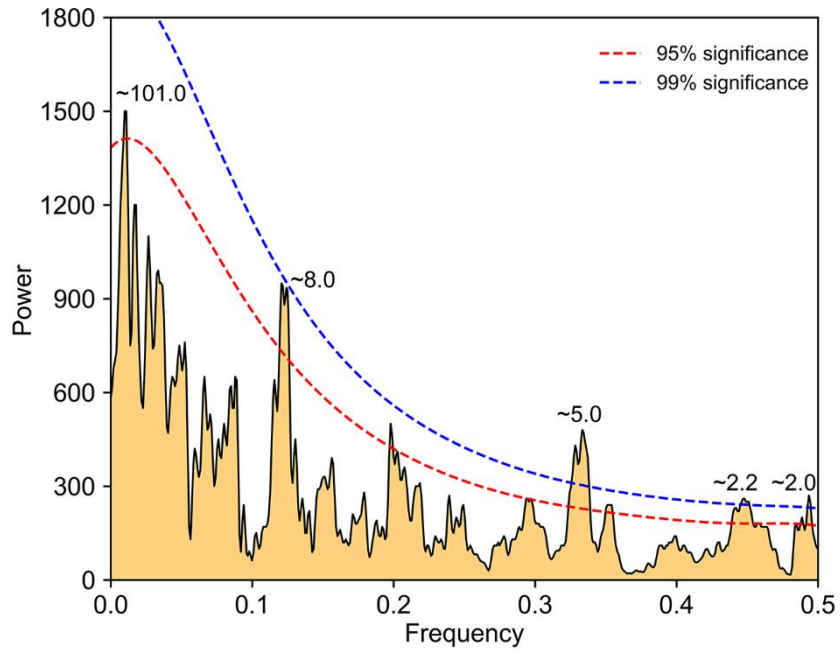
Figure 5. MTM spectral density of the drought reconstruction. The dashed curves represent the 95% (red) and 99% (blue) significance levels, respectively.

622

623
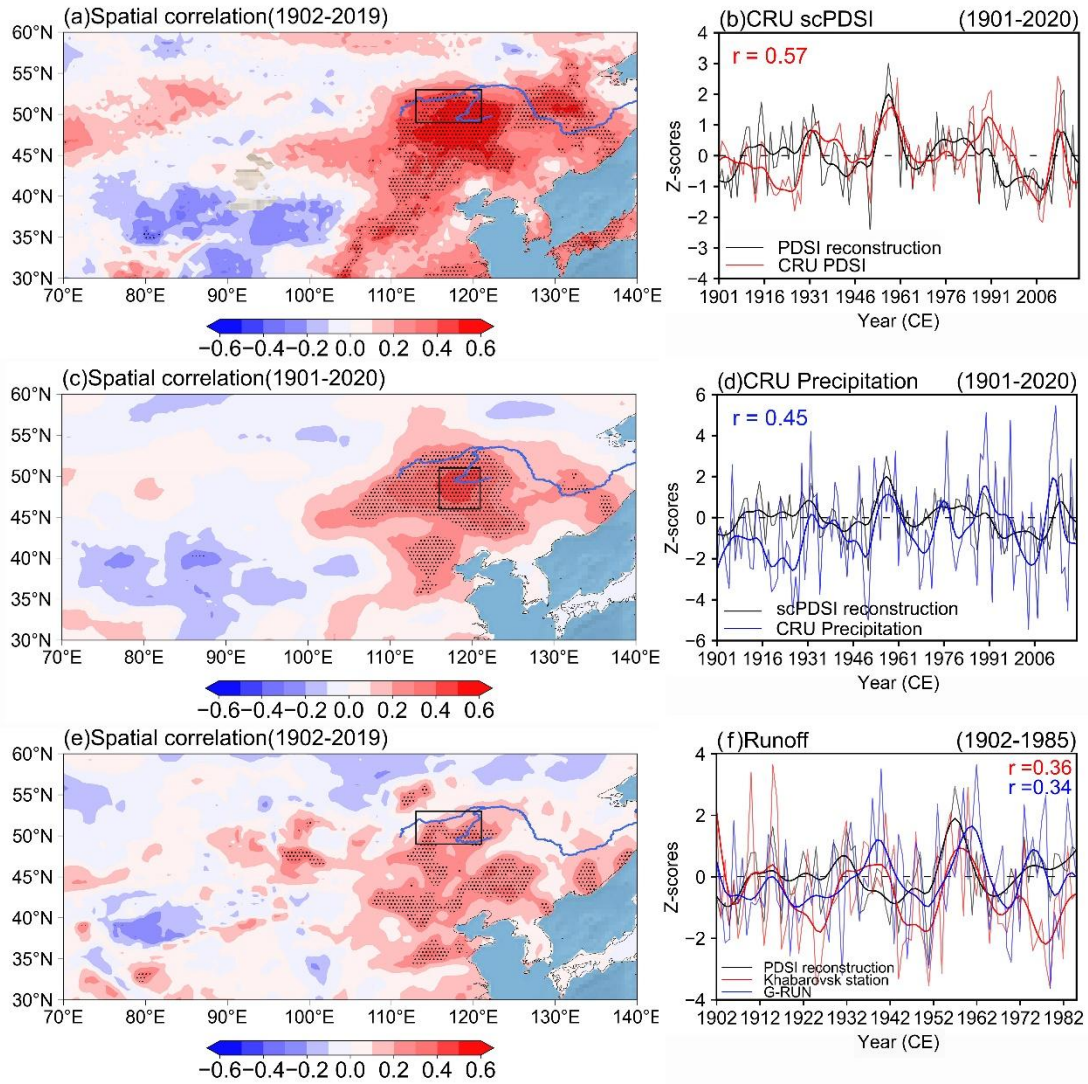
Figure 6. Spatial correlation maps of the reconstructed scPDSI with the CRU gridded
mean May–July scPDSI (a), the CRU gridded total May–July precipitation (c) since
1901 CE. The rectangle indicates the location of the range of the grid, shaded areas
represent the 99% significance level, dark curves represent 10-year low-pass filtered
curves and the same below. The graphs on the right show a comparison of the
reconstructed scPDSI with the regional mean scPDSI (b) and precipitation (d) curves
from the CRU, dark curves represent ten years of low-pass filtering. (e) Reconstructed
scPDSI with G-RUN gridded May-July mean runoff spatial correlation maps for the
period of 1902–2019. (f) Comparison of reconstructed scPDSI, hydrological station
runoff data, and the G-RUN regional mean runoff data for the period of 1902–1985.

634
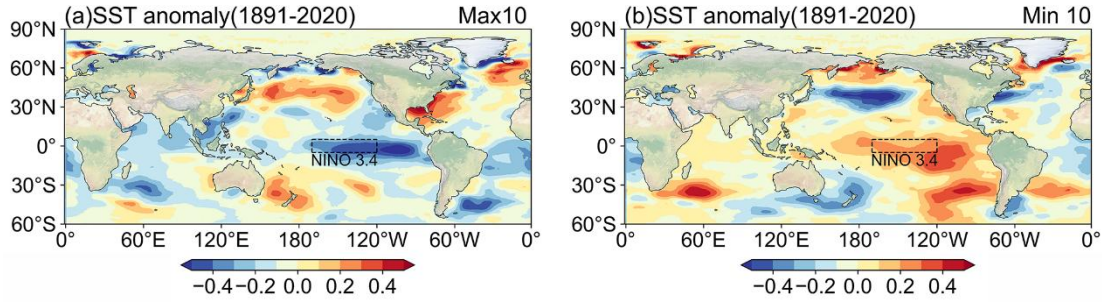
Figure 7. Composite maps of SST anomalies (℃) for the 10 wettest years (a) and 10 driest years (b) from the previous December to the current January during 1891–2020.
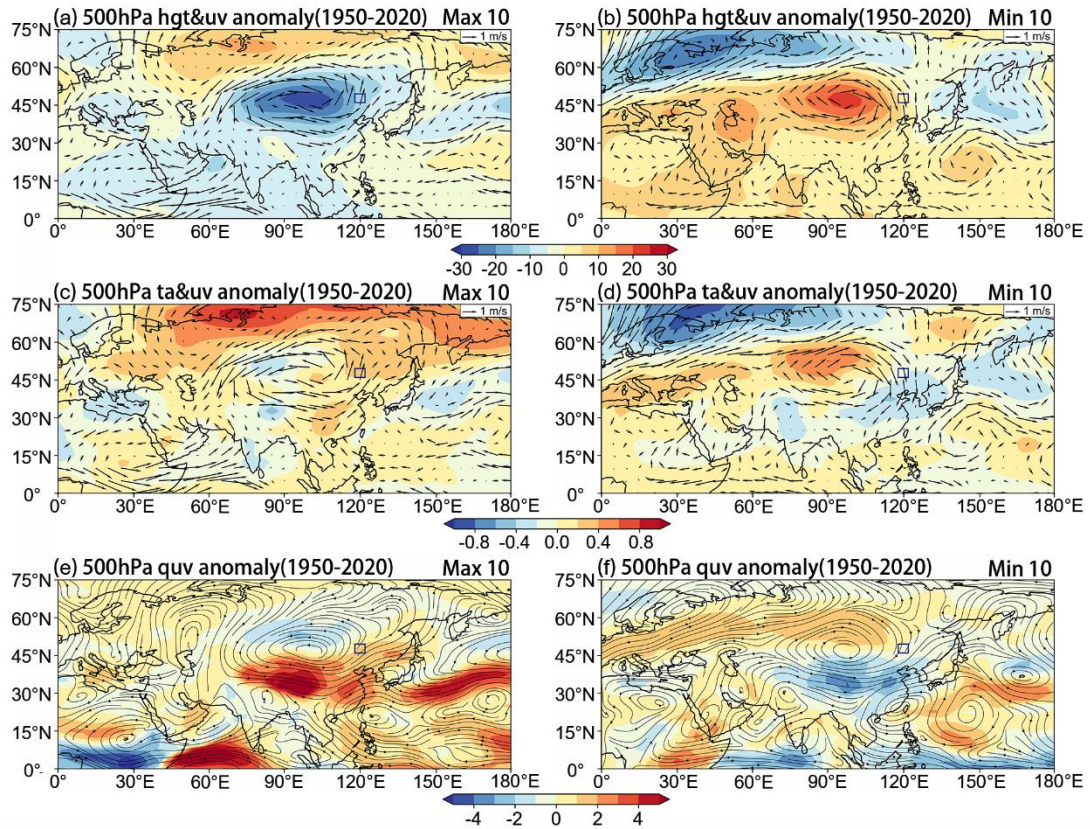
Figure 8. Spatial patterns of geopotential height and 500 hPa vector wind anomalies (a, b), 500 hPa air temperature, and 500 hPa vector wind anomalies (c, d), 500 hPa water vapor transport anomalies (e, f) in the wettest decade and the driest decade during 1950–2020 in NCEP-NCAR Reanalysis 1. The rectangle indicates the location of the study area.

651

652

653 **Figure 9.** (a) Anomaly composites of the mean precipitation rate (kg/s·m^2) and the
654 whole layer moisture flux (kg·m/s) for May–July of the driest decade in the study area
655 (115–125°E, 42.5–52.5°N) relative to that of May-July for the period of 1950–2020
656 (arrows represent the the whole layer moisture flux, filled colors represent the
657 precipitation rate). (b) Schematic diagram of the land-atmosphere water balance in the
658 study area during the climatic period (1950-2020) and dry years. The variables in this
659 plot (i.e., *Fin, Fout-a, Fout-e, Fout, Pa, Pe, P, E*) are explained in Section 2.4. The
660 blue labels (in kg/s) indicate climatic averages, while the red labels indicate averages
661 during drought.

662
663
664
665
666
667
668
669